Korean J. Chem. Eng., 36(1), 56-62 (2019)
DOI: 10.1007/s11814-018-0159-9

pISSN: 0256-1115
eISSN: 1975-7220

Superior dye degradation using SnO_2-ZnO hybrid heterostructure catalysts

Shama Sehar*,†, Iffat Naz, Irum Perveen***, and Safia Ahmed*****

*School of Biotechnology and Biomolecular Sciences, The University of New South Wales, Sydney NSW 2052, Australia
**Department of Biochemistry, Deanship of Educational Services, Qassim University,
Buraidah 51452, Kingdom of Saudi Arabia
***Environmental Microbiology Laboratory, Department of Microbiology, Faculty of Biological Sciences,
Quaid-i-Azam University, Islamabad 45320, Pakistan
(*Received 13 July 2018 • accepted 29 September 2018*)

Abstract−We investigated the efficiency of oxide based hierarchical heterostructure as adsorbent for the treatment of organic dyes, Methyl orange (MO) and Methylene Blue (MB), containing solution. Nanocrystals such as ZnO nanorods (at various temperatures of 30, 60 and 75 °C) and SnO_2 nanoparticles were synthesized by electrodeposition method and hydrothermal approaches, respectively. SnO_2-ZnO heterostructures were formed by spin coating SnO_2 nanoparticles on ZnO nanorods matrix to form a heterostructured film. The surface morphologies and structural characterization of as-prepared heterostructures were investigated by scanning electron microscopy (SEM), transmission electron microscopy (TEM) and X-ray diffraction (XRD) techniques. While, absorption spectra of all samples were examined by UV-vis diffuse reflectance spectroscopy. The photocatalytic activities of as-prepared samples for organic dyes degradation were tested under UV light as model reaction. The SnO_2-ZnO heterostructured photocatalyst showed superior activities than individual ZnO and SnO_2 nanocrystals. This heightened behavior was attributed to its better charge separation capability and the slow charge recombination originating due to difference in energy values of conduction band edges of SnO_2 and ZnO. The SnO_2-ZnO heterostructure demonstrated better stability and recyclability up to five times, which is highly desirable for potential industrial applications including dye degradation and wastewater treatment systems.

Keywords: Organic Dye Degradation, Hydrothermal Approach, Metal Oxide Heterostructures, Photocatalysis, Electrochemical Deposition

INTRODUCTION

Water, being the utmost necessity of life, needs continuous improvement in its quality and preservation of available natural reservoirs. Unfortunately, the continuous addition of undesirable organic and inorganic pollutants from various sources such as industrial discharge, chemical spills and agricultural runoff not only poses serious threats to our existing natural water reservoirs but is equally dangerous to the ecosystem [1,2]. The alarming situation about industrial discharged pollutants is that they are composed of organic and inorganic dyes which are more chemically stable and are resilient to water, sunlight and other basic chemicals making their decomposition even difficult. Furthermore, these dyes can produce intense colorization to the normal water and are poisonous/carcinogenic for human health and marine life [3]. Among organic dye pollutants, Methyl Orange and Methylene Blue (MO and MB) are the largest dyes produced globally in textile, paper, pharmaceutical, cosmetics and leather industries [4-6]. Besides being carcinogenic and mutagenic, their combined toxic effects also include disruption to central nervous systems, respiratory distress, gastrointestinal issues and pulmonary edema for human beings [7,8]. The contaminated wastewater with the above-mentioned dyes has been treated by several non-destructive techniques including adsorption, ultra-filtration, reverse osmosis, or chemical coagulations [9-13]. However, the efficiency of these methods is quite doubtful, as these they are somewhat expensive, slow and produce some secondary pollutants; thus further treatment is needed to remove the byproducts [14]. Photocatalysis has been regarded as one of the green and efficient approaches that can completely remove dye pollutants without producing any byproducts [15-21]. Photocatalysis mainly involves photonic based charge carriers, efficient transmission of an electron/hole as well as their recombination rates. Once the photogenerated charge carriers have been generated, they tend to recombine instantly either on the surface of the particles or in the bulk. However, for greater efficiencies, these photogenerated carriers should be able to generate free radicals by reacting with the absorbed species on the nanoparticles [22]. Therefore, it is believed that by coupling more than one material with different bandgaps, electron affinity and ionization potentials may hinder the issues of fast recombination of the photogenerated electron/hole pairs [23-27].

Usually, complex hierarchical nanostructures are constructed by assembling nanocrystal building blocks such as nanoparticles, nanowires, nanotubes, nanobelts, nanosheets and nanorods. These heterostructures not only increase specific surface area but also provide surface active sites to trap the electrons and holes to retard their recombination rates [28]. In recent years, a wide variety of coupled semiconductor heterostructures such as ZnO-WO_3 [29], ZnO-TiO_2 [30,31], SnO_2-V_2O_5 [32,33], ZnO-SnO_2 [34], have been

†To whom correspondence should be addressed.
E-mail: shamaseher@yahoo.com

extensively investigated for incorporation into photocatalytic reactions. Among various oxides, SnO_2 and ZnO are well-known semiconductors occupying wide direct band gaps (Eg=3.37 and 3.5 eV at 300 K) and potentially utilized in diverse applications ranging from photovoltaics to photocatalysis and gas sensing [35-37]. Furthermore, one-dimensional nano-materials possess more exposed surface area as well as high charge mobility rates [38].

Herein, we report the fabrication of a hierarchical nanostructure composed of SnO_2 nanoparticles on ZnO nanorods arrays for organic dye degradation. First, ZnO nanorods array matrix was fabricated to act as a baseline of the hierarchical heterostructure. Subsequently, ultra-small (~5-8 nm) SnO_2 nanoparticles were synthesized via hydrothermal process. Finally, the SnO_2-ZnO heterostructure was formed by spin-coating SnO_2 nanoparticles over ZnO matrix. The photocatalytic activity of the individual nanostructures (ZnO, SnO_2) as well as the SnO_2-ZnO heterostructure was evaluated by measuring the degradation abilities of organic dyes (Methyl Orange (MO) and Methylene Blue (MB) under UV irradiation. The photocatalytic properties of the SnO_2-ZnO-based catalysts were found to be superior to individual nanostructures, and their enhanced efficiency was addressed based on better charge separation phenomenon. The heterostructure proposed in this report can potentially be applied in various environmental and industrial related sectors.

MATERIALS AND METHODS

1. Synthesis of ZnO Nanorods

All chemicals of analytical grade (99.95% purchased from sigma Aldrich) were used throughout this study. ZnO nanorods are prepared by electrodeposition method with the use of HA151 Potentiostat (Hokuto Denko). Three-electrodes were used, where fluorine tin oxide glass substrate FTO was used as working electrode, platinum foil was used as counter electrode and Ag/AgCl electrode in 4 M KCl solution as reference electrode. Prior to deposition, the substrate was cleaned with ethanol followed by acetone and then dried under nitrogen air flux. The electrodeposition was carried out in a solution of 0.01 M Zn $(NO_3)_2 \cdot 6H_2O$ at 2 mA for 30 min, at various temperature ranges (30 °C, 60 °C and 75 °C) respectively.

2. Synthesis of SnO_2 Nanoparticles

The SnO_2 nanoparticles were synthesized by hydrothermal approach. Typically, the aqueous solution of 12 ml of 13.5 mmol/*l* Tin (IV) nitrate was added into a 50 ml autoclave. In another beaker, a mixed solution of 15 ml toluene, 0.5 ml oleic acid and tert-butylamine (0.10 ml) was prepared. After 30 minutes, both solutions were mixed together and put in an autoclave for 36 hours at 200 °C. Once, the mixture was cooled at room temperature, the product was extracted, centrifuged and washed several times with ethanol and deionized water.

3. Synthesis of SnO_2-ZnO Heterostructures

The SnO_2-ZnO heterostructures were formed by spin coating SnO_2 suspension on already formed ZnO nanorod array film. For convenience, the electrodeposited samples (ZnO@30 °C, ZnO@60 °C and ZnO@75 °C) were named as S-1, S-2 and S-3 afterwards. The heterostructure (Spin coated SnO_2 on S-3) sample is named as S-4 onwards.

4. XRD Characterization

The crystal structure and phase composition of the samples were characterized by X-ray powder diffraction (Philips X'pert Multipurpose (MRD) with Cu Kα source (1.5418 Å). The diffraction pattern was collected for 2-Theta range between 20°-80° with a scan speed of (0.001°/s).

5. Scanning and Transmission Electron Microscopic Analysis (SEM and TEM)

The microstructures (Surface morphologies) of as-prepared nanostructures were obtained using Nova SEM 230 and transmission electron microscope (Philips CM200) operating at 200 kV.

6. Brunauer-Emmett-Teller (BET) Surface Area Measurements

The Brunauer-Emmett-Teller (BET) specific surface area was evaluated by N_2 absorption-desorption at low temperature (close to liquid nitrogen temperature) on a Micromeritics Tristar 3030. To remove the excessive moistures, the samples were pre-treated under vacuum conditions for 3 hours at 150 °C.

7. Photocatalytic Degradation of Dyes

The photocatalytic activity of all samples was investigated by the degradation of organic dyes Methyl Orange (MO) and Methylene Blue (MB) dye under UV irradiation. First, a dye solution (MO and MB) of 15.5 mg/*l* (total 100 ml) was formed, then 15 mg of photocatalyst (S-1, S-2 and S-3) was added to the solution. The beaker containing mixed solution of dye and photocatalysts was placed locally under the UV light source (15 cm apart). Prior to UV irradiation, the solution was stirred for 30 min to attain adsorption/desorption equilibrium.

After irradiation with UV light, 5 ml aliquots were collected and subjected to centrifugation (at 4,000 rpm for 10 min) to ensure complete removal of catalyst particles. The supernatant was collected and used to determine the concentration of residual dye by UV-vis spectroscopy (PerkinElmer) at 464 and 610 nm for MO and MB, respectively. The entire procedure was triplicated for each sample. For calculating percentage degradation of organic dyes, the following equation was used [39,40]:

$$\text{Degradation rate (\%)} = \left(\frac{C_o - C}{C_o}\right) \times 100$$

where, C_o is the initial dye concentration, C is the dye concentration after UV irradiation. We used the same conditions to recycle and reuse the catalysts for five batches.

RESULTS AND DISCUSSION

1. Morphology and Microstructural Analysis

The surface morphologies of as-ZnO nanostructures, (S-1, S-2, S-3) fabricated on FTO through SEM are presented in Fig. 1. At electrodeposited temperature of 30 °C for ZnO, irregular shaped ZnO nano-micro particles/flakes with diverse diameter range were formed as shown in Fig. 1(a). In a general electrodeposition process, first hydroxyl ions are formed on the substrate surface by reducing nitrate precursors in zinc ions aqueous solution [41]. The presence of Zn^{2+} ions serves as catalysis for the electrochemical reduction of nitrate ions which may then absorbed on cathode's surface to liberate hydroxide ions [42].

A further increase in the reaction temperature (60 °C) leads to the formation of ZnO nanorods with an average diameter of 50-80 nm as shown in Fig. 1(b). The transformation of ZnO nano-micro parti-

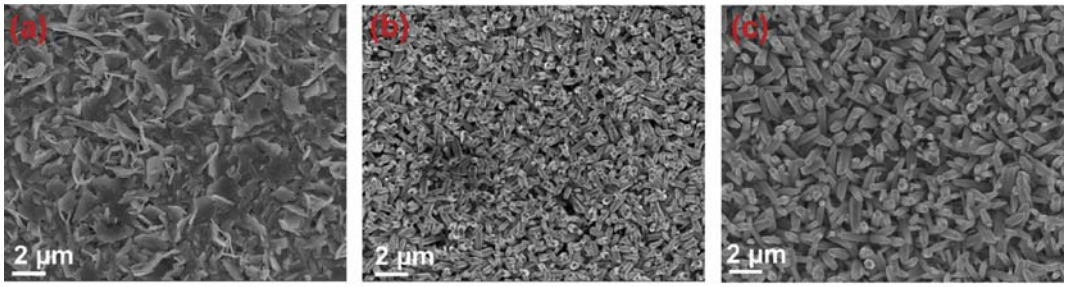

Fig. 1. Surface morphology of as-synthesized nanocrystals: SEM image of electrodeposited ZnO (a) at 30 °C (b) 60 °C (c) 75 °C.

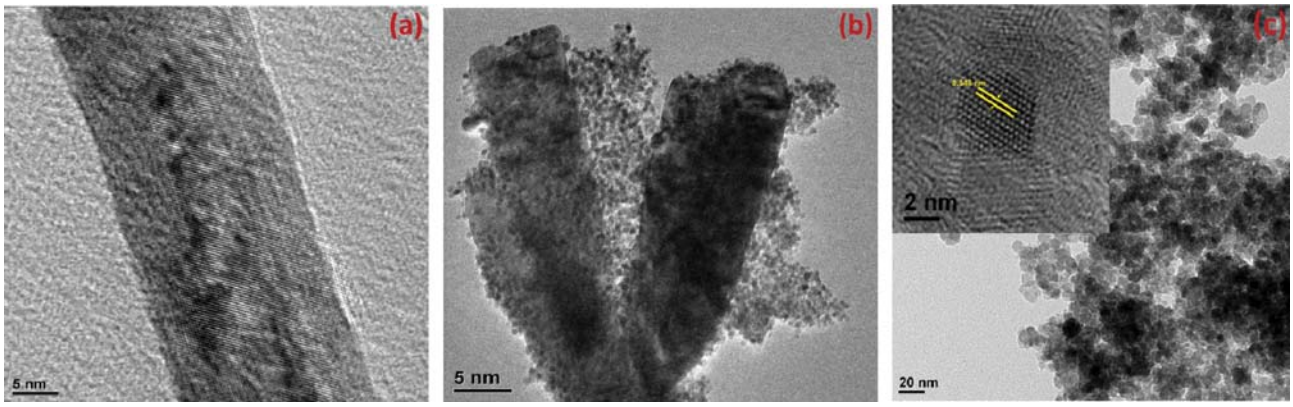

Fig. 2. (a) TEM of a single ZnO nanorod synthesized at 75 °C (b) TEM of ZnO-SnO_2 heterostructure, (c) TEM image of dispersed SnO_2 nanoparticles, inset HRTEM of a single SnO_2 nanoparticles clearly showing lattice fringes.

cles/flakes to nanorods is an indication of the formation of pure ZnO phase. The elevated temperature (60 °C) favors the spontaneous dehydration of zinc hydroxide to form zinc oxide nanocrystal as shown in Fig. 1(b). By further increasing reaction temperature to 75 °C, the ZnO nanostructures maintain their surface morphology of nanorods with well-organized, and dense nanorods arrays appeared perpendicular to the substrate surface as shown in Fig. 1(c). The ZnO prefers to grow along (001) owing to its lowest surface energy in aqueous solution. Therefore, the growth in [010] direction is much slower than [001] direction, which results in the formation of nanorod arrays. The transmission electron microscopy (TEM) image of a single ZnO nanorod (S-3) is illustrated in Fig. 2(a). The diameter of the single rod was observed to be around ~100 nm. Fig. 2(b) shows the SEM image of the SnO_2-ZnO heterostructure. It can be clearly observed that the ZnO nanorods are well covered with the SnO_2 nanoparticles of 5-10 nm diameter. Moreover, the highly dispersed SnO_2 nanoparticles can be found in Fig. 2(c); the size of each nanoparticle was found to be in the range of 5-10 nm (inset of Fig. 2(c)). It is quite clear that the SnO_2 nanoparticles surrounded the ZnO nanorods and hence the heterostructure was confirmed. Moreover, in the HRTEM micrographs (inset of Fig. 2(c)) the interplanar spacing of 0.348 nm was observed, which corresponds to the (110) plane of rutile SnO_2, which was further confirmed through XRD measurements as well.

The crystalline structure of the as-prepared samples (S-3 and S-4) was examined by x-ray diffraction as shown in Fig. 3. The diffraction spectra showed clear, sharp, and strong diffraction peaks, and the diffracted peaks match well with the standard hexagonal

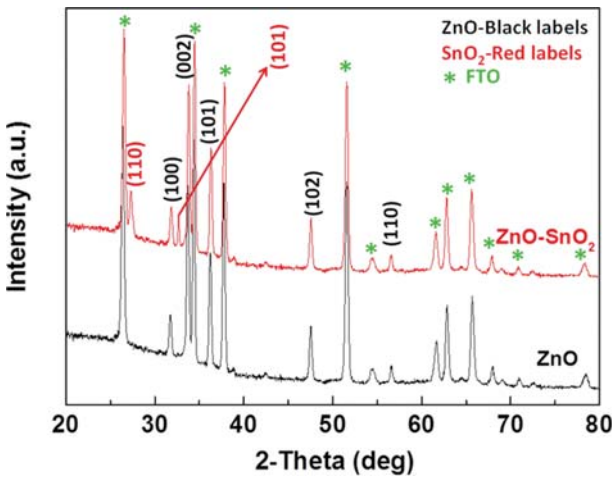

Fig. 3. XRD patterns of the electrodeposited ZnO at 75 °C and SnO_2-ZnO heterostructure.

wurtzite phase of ZnO (JCPD # 36-1451) and standard rutile-like structure of SnO_2 (JCPD # 41-1445), respectively. Furthermore, no impurity peaks related to unreacted Zn, Sn or other oxides of these elements were observed, which is a clear indication of the formation of pure ZnO and SnO_2 nanocrystals.

A bulk composition analysis of SnO_2-ZnO heterostructure was carried out through energy-dispersive X-ray spectroscopy (EDX), as shown in supporting information, Fig. S1. From (Fig. S1), it can be confirmed that the SnO_2-ZnO heterostructure is composed of

Zn, Sn, and O, which was consistent with the XRD analysis. In addition, EDX analysis indicated that the molar ratio of Zn to Sn was 1 : 0.9, which was close to the theoretical value.

2. Surface Composition Analysis

To investigate the surface composition and chemical states of as-prepared SnO_2-ZnO heterostructure, XPS analysis was conducted and the results are in Fig. 4. The XPS survey scan clearly show the peaks related to Zn, Sn and O (Fig. 4(a)). The binding energy at 1,022.3 eV (Fig. 4(b)) is identified as Zn $2p_{3/2}$, indicating a normal state of Zn^{2+} in the SnO_2-ZnO hierarchical structures [43]. The Sn 3d spectrum of the sample (Fig. 4(c)) appears as a spin-orbit doublet at ~486.2 eV ($3d_{5/2}$) and ~491.3 eV ($3d_{3/2}$) and is in good agreement with the values given in literature [44]. Three peaks at 529.8, 532.4 and 533.9 eV can be observed in O 1s XPS spectra (Fig. 4(d)). The peak at 529.8 may be the character spectra of oxygen in SnO_2-ZnO structure [45]. The peak at 532.4 eV can be assigned to the lattice oxygen [46]. Whilst the O peak at 533.9 eV may be attributed to chemisorbed oxygen ions present in the sample [47]. The chemisorbed oxygen impurities could be O_2^-, O^-, O_2^{-1} ,O_2^{2-} and OH^- ions as well [48,49], so the binding energy not only depends on the charge of oxygen species but also upon the crystallographic orientation of the bounded surface to which the oxygen atoms or molecules are bound [48], which points to the nonstoichiometric nature and presence of oxygen vacancies in the sample.

3. Photocatalytic Performance

The photocatalytic activity of as prepared SnO_2-ZnO nanocrystals (S-1, S-2, S-3 and S-4) was examined by the photodegradation of organic dyes [anionic dye (Methyl Orange, MO) and cationic dye (Methyl Blue, MB)] and the results are depicted in Fig. 5(a) and 5(b). For a typical experiment, 3 mg of as-prepared catalyst was

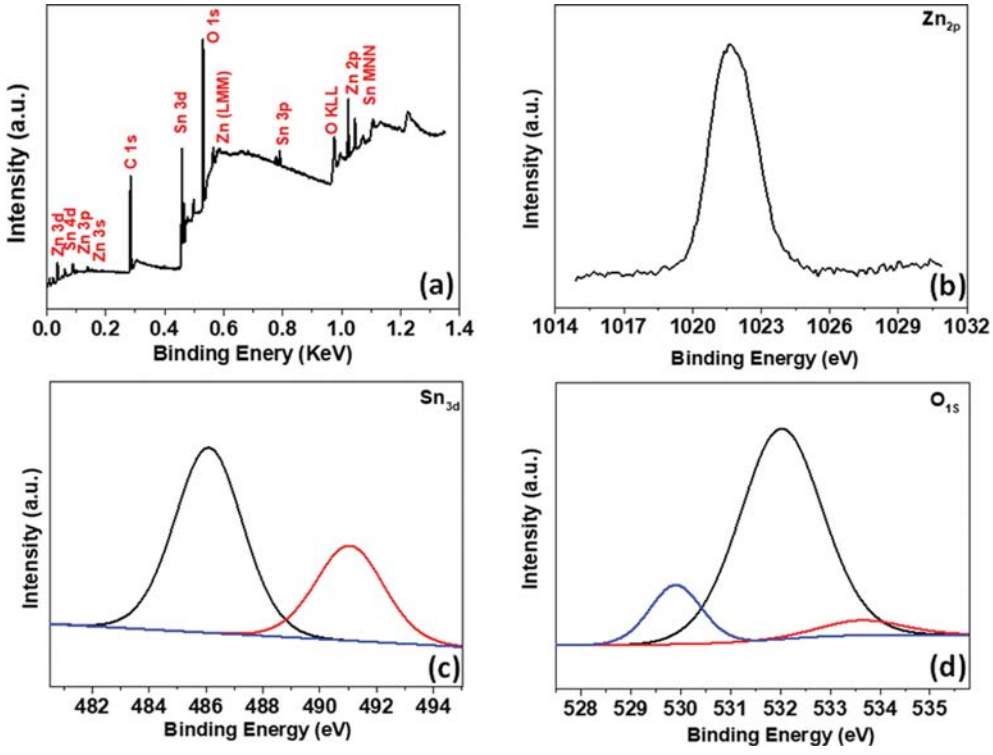

Fig. 4. XPS spectra of the SnO_2-ZnO heterostructure: (a) Survey (b) Zn 2p spectra; (c) Sn 3d spectra; (d) O 1s spectra.

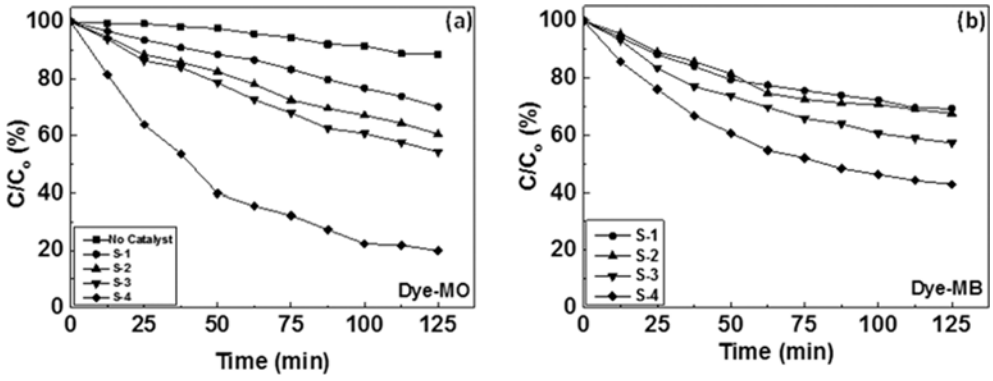

Fig. 5. Photocatalytic degradation of (a) MO and (b) MB with different ZnO samples S-1, S-2, S-3 and S-4.

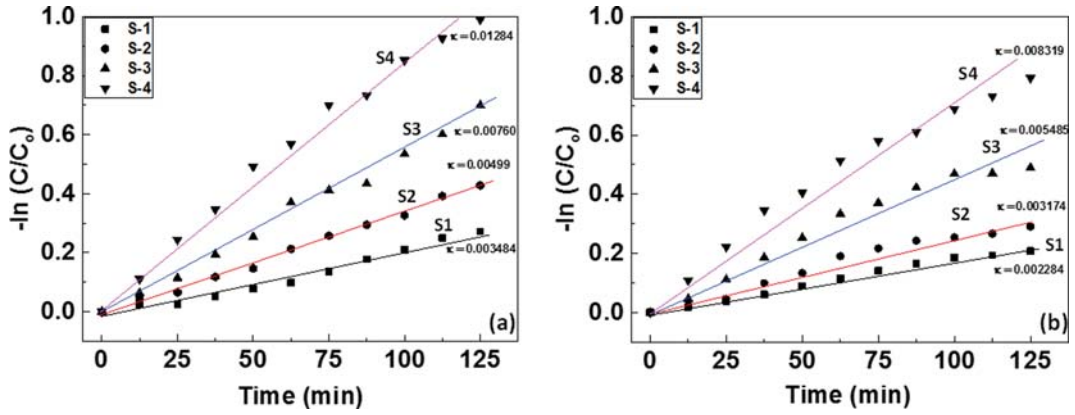

Fig. 6. Plots of $-\ln(C/C_0)$ vs irradiation time at room for all samples to determine rate constant for (a) MO and (b) MB dyes. The black, red, blue and pink lines indicate the straight lines for slope calculations.

added in the dye solution (12.5 mg/*l* dye solution). The photocatalytic dye degradation efficiencies of the as-prepared samples were investigated for 125 minutes. A control experiment in which only SnO_2 nanoparticles were used as photocatalyst was also conducted and the results are in Fig. S2 (supporting information). The dye degradation efficiency of MO was also evaluated without adding any photocatalyst (Fig. 5(a)). Almost no dye decolorization was observed throughout the course of reaction time (125 minutes), which indicates that UV light itself cannot degrade dye solution. An increasing trend in photocatalytic dye decolorization efficiency of ZnO nanocrystals was observed. The samples prepared at 75 °C were found to decolor MO faster than for the photocatalyst prepared at lower temperatures (30 and 60 °C). The degradation efficiency of S-3 at 125 minutes reaction time was around 40%, while S-1 and S-2 decolor MO about 22% and 29%, respectively. Even the dye degradation ability of SnO_2 is not better than ZnO (supporting information S2). However, the SnO_2-ZnO samples (S-4) were found to express superior performance in dye degradation over two individual materials (SnO_2 and ZnO, S-1, S-2 and S-3, respectively). This clearly shows that the presence of two phases imposes some synergistic effect (Fig. 5(a)) to obtain enhanced photocatalytic performance. The SnO_2-ZnO heterostructure (S-4) exhibited the highest photocatalytic efficiency and almost degraded ~80% of MO dye solution in 125 minutes of reaction time.

The investigation of cationic dye degradation (MB) in the presence of all nanocrystals (S-1, S-2, S-3 and S-4) was also carried out as shown in Fig. 5(b). As expected, the sample S-4 degraded MB much faster than other catalysts (in the same manner as for the case of MO). However, the overall catalytic efficiency of S-4 was much higher for anionic dye degradation (MO) (80% degradation) than the cationic dye (MB) (55%) degradation. This difference in catalytic activity for the case of anionic and cationic dye may be attributed to the pH of the medium and the isoelectric points of catalysts. For a higher pH of the solution than the isoelectric point of catalyst material, the surface becomes negatively charged (since the isoelectric point of zinc oxide lies between 8.7-10.3 [50] and for lower pH than the isoelectric, the surface becomes positively charged. This could be a possible reason for higher degree of dye degradation efficiency in our samples observed for anionic dyes.

The decomposition dynamics of MO and MB in the presence of S-4 is recorded and plotted in Fig. 6(a) and 6(b), and they clearly followed pseudo-first order reaction. Sample S-4 degraded dye MO much faster than MB ((decomposition rates ~0.01284/min and 0.008319/min, respectively). Note that non-stoichiometry/oxygen vacancies at high temperatures become more mobile with low probability to form deep trap sites. Therefore, a higher catalytic efficiency is expected at elevated temperatures. To demonstrate this concept experimentally, the degradation efficiency of MO was recorded at high temperatures (from 30 °C up to 100 °C) as shown in supporting information, Fig. S3. The catalyst S-4 degraded the dye faster at higher temperatures than at room temperature. This profound dye degradation ability at high temperatures may be attributed to the phonon scattering effects and increased oxygen ionic mobilities. The electrons/holes can easily get scattered with the lattice vibrations at higher temperatures, which restricts the electron-hole recombination process.

The recyclability and reusability of S-4 for several cycles was tested for five cycles as shown in Fig. 7. Although the degradation efficiency slightly decreased after the fifth run (less than 5%), the

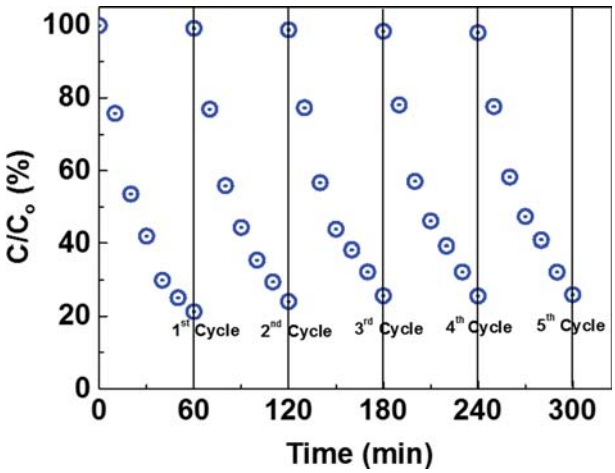

Fig. 7. Cycling runs of MO decolourisation using SnO_2-ZnO heterostructure.

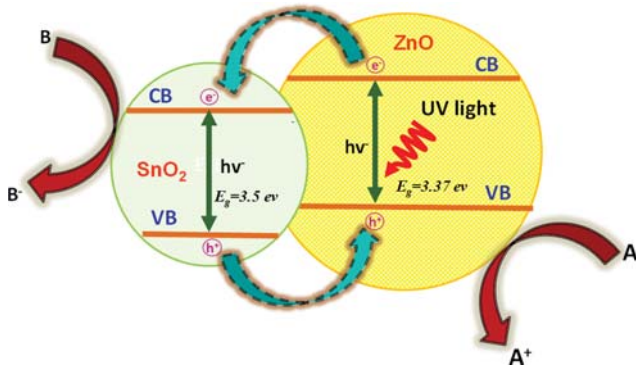

Fig. 8. Schematic diagram of the degradation mechanisms for the MO dye with SnO_2-ZnO heterostructure under ultraviolet-visible light irradiation.

SnO_2-ZnO catalyst remained effective and reusable under UV light irradiation.

Based on the above experimental results, we propose the following possible photocatalytic process for the SnO_2-ZnO heterostructure (schematically shown in Fig. 8). The enhanced photocatalytic activity of the SnO_2-ZnO (S-4) heterostructure over other nanocrystals may be attributed to the transfer of photogenerated electrons.

When the heterostructure is exposed with UV-light, electrons from valence bands (VB) are excited to the conduction band (CB) by generating similar amount of VB holes. Photogenerated electrons are then injected from the CB of the ZnO to the CB of SnO_2 (Fig. 8). Simultaneously, holes are injected in the opposite direction for appropriate VB offsets, thus increasing the rate of charge separation by prolonging the recombination rate of electron-hole pairs. Moreover, for SnO_2-ZnO based heterostructure, both holes and electrons are accessible for selective oxidation and reduction processes on the surface of both semiconductors [36,51].

In addition, it is widely known that most heterogeneous catalysis between the catalysts and reactants occurs on the surface or at the interface, so the photocatalytic activity partly depends on the specific surface area of materials [39,52]. Therefore, Brunauer-Emmett-Teller (BET) surface areas of all samples were calculated and the sample S-4 was found to exhibit highest surface area than other samples (supporting information Fig. S4). Being occupying highest surface area, S-4 possesses excellent dye degradation ability too. Large surface areas can provide more active sites to form oxidative hydroxyl radicals by reacting with absorbed water and hydroxyl radicals [53,54]. Thus, a superior dye degradation efficiency was observed for the case of S-4 over other photocatalyst. Moreover, the UV-vis diffuse reflectance (DR) spectra of all samples were carried out to estimate the band gap energies (Fig. S5). From figure, it is clear that S-4 occupied lowest band gap energy, which may be another reason for the enhanced photocatalytic activity of S-4 over other samples.

CONCLUSIONS

We have synthesized a series of ZnO based samples from facile wet-chemical routes of electrochemical deposition and hydrothermal approach. Among all prepared samples, SnO_2-ZnO heterostructure expressed superior photocatalytic activity for organic dyes degradation under UV light irradiation. The highest surface area and modified band alignment for heterostructure facilitate to prolong the electron-hole recombination process, which were highlighted as main route cause for the enhanced photocatalytic activities. Moreover, the heterostructure photocatalysts have shown great tendency for recycling and reusability without sacrificing performance. This concept of forming semiconducting heterojunctions with improved photocatalytic activity can potentially be applied in future industrial applications as well as wastewater treatment technologies to remove undesirable organic waste.

ACKNOWLEDGEMENT

The authors would like to greatly acknowledge support from the electron microscope unit of UNSW for providing SEM and TEM facilities.

CONFLICT OF INTEREST

The authors declare no financial or any other conflict of interest.

SUPPORTING INFORMATION

Additional information as noted in the text. This information is available via the Internet at http://www.springer.com/chemistry/journal/11814.

REFERENCES

1. M. S. Diaz-Cruz and D. Barcelo, *Chemosphere*, **72**, 333 (2008).
2. U. G. Akpan and B. H. Hameed, *J. Hazard. Mater.*, **170**, 520 (2009).
3. H. Zhao, G. Zhang, S. Chong, N. Zhang and Y. Liu, *Ultrason. Sonochem.*, **27**, 474 (2015).
4. R. Kumar, G. Kumar, M. S. Akhtar and A. Umar, *J. Alloys Compd.*, **629**, 167 (2015).
5. N. B. Bokhale, S. D. Bomble, R. R. Dalbhanjan, D. D. Mahale, S. P. Hinge, B. S. Banerjee, A. V. Mohod and P. R. Gogate, *Ultrason. Sonochem.*, **21**, 1797 (2014).
6. K. Rastogi, J. N. Sahu, B. C. Meikap and M. N. Biswas, *J. Hazard. Mater.*, **158**, 531 (2008).
7. P. K. Gillman, *J. Psychopharmacol.*, **25**, 429 (2011).
8. D. T. Sponza, *Enzyme Microb. Technol.*, **31**, 102 (2002).
9. D. Ozer, G. Dursun and A. Ozer, *J. Hazard. Mater.*, **144**, 171 (2007).
10. A. El Sikaily, A. Khaled, A. El Nemr and O. Abdelwahab, *Chem. Ecol.*, **22**, 149 (2006).
11. M. Moradi, F. Ghanbari, M. Manshouri and K. A. Angali, *Korean J. Chem. Eng.*, **33**, 539 (2016).
12. W. S. W. Ngah, L. C. Teong and M. A. K. M. Hanafiah, *Carbohydr. Polym.*, **83**, 1446 (2011).
13. K. Singh and S. Arora, *Crit. Rev. Environ. Sci. Technol.*, **41**, 807 (2011).
14. T. Warang, N. Patel, R. Fernandes, N. Bazzanella and A. Miotello, *Appl. Catal. B Environ.*, **132-133**, 204 (2013).
15. H. Hung, F. H. Ling and M. R. Haffmann, *Environ. Sci. Technol.*, **34**, 1758 (2000).

16. A. Hassani, R. D. C. Soltani, Murat Kıranşan, S. Karaca, C. Karaca and A. Khataee, *Korean J. Chem. Eng.*, **33**, 178 (2016).
17. A. Hassani, M. Kiransan, R. D. C. Soltani, A. Khataee and S. Karaca, *Turk. J. Chem.*, **39**, 734 (2015).
18. N. Modirshahla, M. A. Behnajady, R. Rahbarfam and A. Hassani, *Clean (Weinh)*, **40**, 298 (2012).
19. A. Hassani, P. Eghbali, A. Ekicibil and O. Metin, *J. Magn. Magn. Mater.*, **456**, 400 (2018).
20. A. Hassani, G. Çelikdağ, P. Eghbali, M. Sevim, S. Karaca and O. Metin, *Ultrason. Sonochem.*, **40**, 841 (2018).
21. A. Younis, S. Shirsath, B. Shabbir and S. Li, *Nanoscale*, **10**, 18576 (2018).
22. L. G. Devi and R. Kavitha, *Appl. Catal. B.*, **140-141**, 559 (2013).
23. D. Y. R. Castanedo Perez, G. Torres Delgado and O. Zelaya Angel, *J. Photochem. Photobiol.*, **235**, 49 (2012).
24. H. Uchiyama, R. Nagao and H. Kozuka, *J. Alloys Compd.*, **554**, 122 (2013).
25. A. Hamrouni, H. Lachheb and A. Houas, *Mater. Sci. Eng. B.*, **178**, 1371 (2013).
26. W. Tian, C. Zhang, T. Zhai, S. L. Li, X. Wang, J. Liu, X. Jie, D. Liu, M. Liao, Y. Koide, D. Golberg and Y. Bando, *Adv. Mater.*, **26**, 3088 (2014).
27. Z. Zhang, C. Shao, X. Li, L. Zhang, X. Hongmei, W. Changhua and Y. Liu, *J. Phys. Chem. C.*, **114**, 7920 (2010).
28. C. Zhang, W. Tiabn, Z. Xu, X. Wang, J. Liu, S. L. Li, D. M. Tang, D. Liu, M. Liao, Y. Bando and D. Golberg, *Nanoscale.*, **6**, 8084 (2014).
29. Y. U. Changlin, K. Yang, S. H. U. Qing, C. Y. J. Jimmy, C. A. O. Fangfang and L. I. Xin, *Chin. J. Catal.*, **32**, 555 (2011).
30. G. Marcì, V. Augugliaro, M. J. López-Munõz, C. Martín, L. Palmisano, V. Rives, M. Schiavello, R. J. D. Tilley and A. M. Venezia, *J. Phys. Chem. B.*, **105**, 1026 (2001).
31. C. Shifu, Z. Wei and L. Z. Sujuan, *Appl. Surf. Sci.*, **255**, 2478 (2008).
32. S. Mathur and S. Barth, *Small*, **3**, 2070 (2007).
33. R. Ostermann, D. Li, Y. Yin, J. T. McCann and Y. Xia, *Nano Lett.*, **6**, 1297 (2006).
34. N. Modirshahla, A. Hassani, M. A. Behnajady and R. Rahbarfam, *Desalination*, **271**, 187 (2011).
35. J. S. Lee, O. S. Kwon and J. Jang, *J. Mater. Chem.*, **22**, 14565 (2012).
36. L. Zhang, L. Yin, C. Wang, N. Lun and Y. Qi, *ACS Appl. Mater. Interfaces*, **2**, 1769 (2010).
37. C. Cheng, B. Liu, H. Yang, W. Zhou, L. Sun, R. Chen, S. F. Yu, J. Zhang, H. Gong, H. Sun and H. J. Fan, *ACS Nano*, **3**, 3069 (2009).
38. W. H. Hui, D. Kong, Z. Ruan, P. C. Hsu, S. Wang, Z. Yu, J. C. Thomas, L. Hu, S. Fan and C. Yi, *Nat. Nanotech.*, **8**, 421 (2013).
39. K. Saeed, G. Ali, I. Khan and H. Khan, *J. Chem. Eng. Chem. Res.*, **2**, 671 (2015).
40. S. Valizadeh, M. H. Rasoulifard and M. S. S. Dorraji, *Korean J. Chem. Eng.*, **33**, 481 (2016).
41. S. Jing, A. Younis, D. Chu and S. Li, *SAIMS Mater. Sci.*, **2**, 28 (2015).
42. X. Feng, L. Yinong, X. Lili, X. Yan, D. Min and L. Yunfei, *Mater. Res. Bull.*, **44**, 1700 (2009).
43. Z. Zhang, C. Shao, X. Li, L. Zhang, H. Xue, C. Wang and Y. Liu. *J. Phys. Chem. C.*, **114**, 7920 (2010).
44. H. J. Ahn, H. C. Choi, K. W. Park, S. B. Kim and Y. E. Sung, *J. Phys. Chem. B.*, **108**, 9815 (2004).
45. M. N. Islam, T. B. Ghosh, K. L. Chopra and H. N. Acharya, *Thin Solid Films*, **280**, 20 (1996).
46. C. D. Wagner, W. M. Riggs, L. E. Davis, J. F. Moulder and G. E. Muilenberg, Handbook of X-ray Photoelectron Spectroscopy, Perkin- Elmer Corporation, Eden Prarie, MN (1979).
47. J. N. Kim, K. S. Shin, D. H. Kim, B. O. Park, N. K. Kim and S. H. Cho, *Appl. Surf. Sci.*, **206**, 119 (2003).
48. S. A. Studenikin, N. Golego and M. Cocivera, *J. Appl. Phys.*, **87**, 2413 (2000).
49. V. E. Henrich and P. A. Cox, The Surface Science of Metal Oxides, Cambridge Univ. Press, Cambridge, UK (1994).
50. R. Marsalek, *APCBEE Procedia.*, **9**, 13 (2014).
51. R. J. Tayade, T. S. Sivakumar and H. C. Bajaj, *Indus. Eng. Chem. Res.*, **48**, 10262 (2009).
52. A. Younis, D. Chu, Y. V. Kaneti and S. Li, *Nanoscale*, **8**, 378 (2016).
53. J. B. Joo, Q. Zhang, M. Dahl, I. Lee, J. Goebl, F. Zaera and Y. Yin, *Ener. Environ. Sci.*, **5**, 6321 (2012).
54. H. Cheng, J. Wang, Y. Zhao and X. Han, *RSC Adv.*, **4**, 47031 (2014).

Supporting Information

Superior dye degradation using SnO_2-ZnO hybrid heterostructure catalysts

Shama Sehar*,†, Iffat Naz, Irum Perveen***, and Safia Ahmed*****

*School of Biotechnology and Biomolecular Sciences, The University of New South Wales, Sydney NSW 2052, Australia
**Department of Biochemistry, Deanship of Educational Services, Qassim University,
Buraidah 51452, Kingdom of Saudi Arabia
***Environmental Microbiology Laboratory, Department of Microbiology, Faculty of Biological Sciences,
Quaid-i-Azam University, Islamabad 45320, Pakistan
(*Received 13 July 2018 • accepted 29 September 2018*)

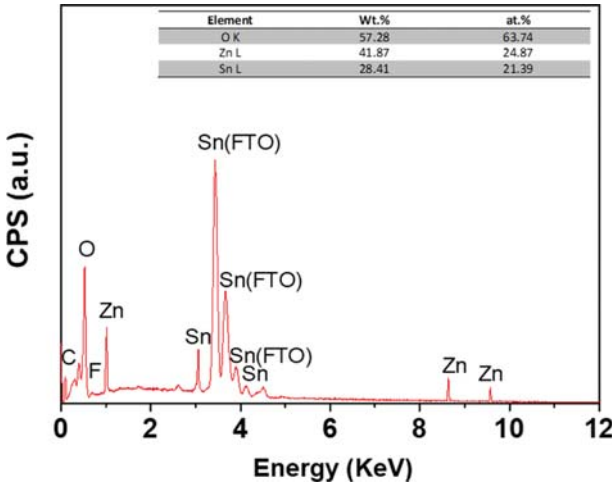

Fig. S1. Elemental analysis of the hierarchical SnO_2-ZnO nanostructures.

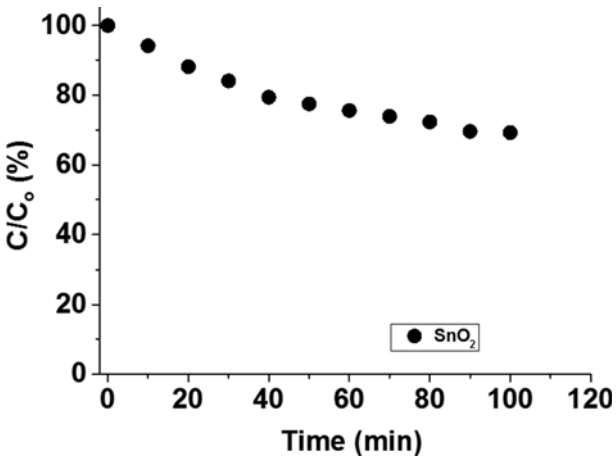

Fig. S2. Photocatalytic degradation of MO in the presence of SnO_2 nanoparticles.

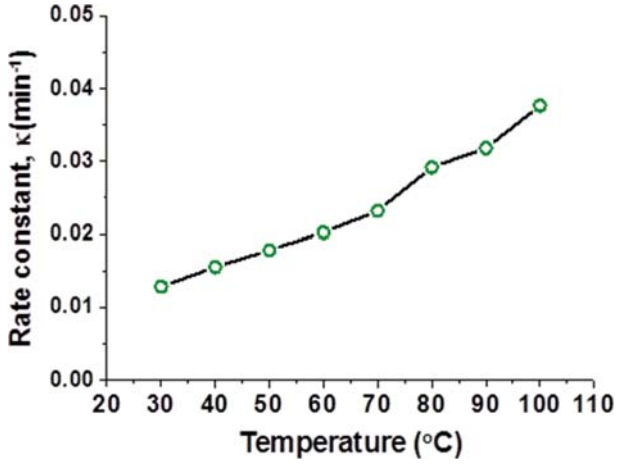

Fig. S3. Temperature dependent rate constant values of S-4 for MO dyes.

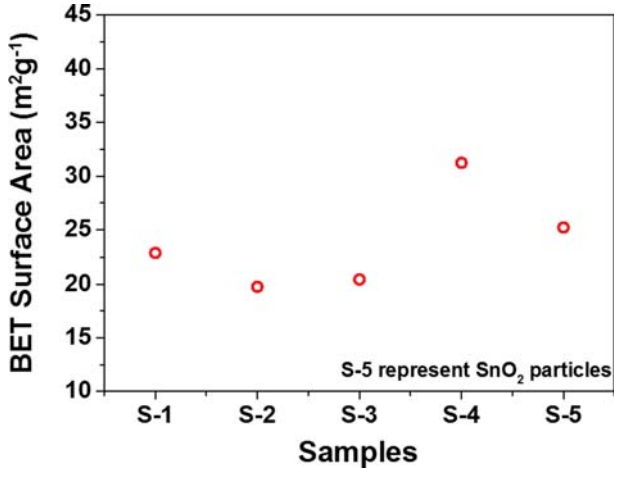

Fig. S4. BET surface areas of all samples.

UV-vis Diffuse Reflectance (DR) Spectroscopy

The UV-vis diffuse reflectance (DR) spectra of the ZnO, SnO_2, and SnO_2-ZnO heterostructure were carried out as shown in Fig. S5. In the absorption edges of ZnO and SnO_2 appeared at 381 and 362 nm, corresponding to band gap energies of 3.25 and 3.42 eV, respectively. Those values were close to the reported value of ZnO (3.37 eV) and SnO_2 (3.5 eV) [1]. For SnO_2-ZnO heterostructure,

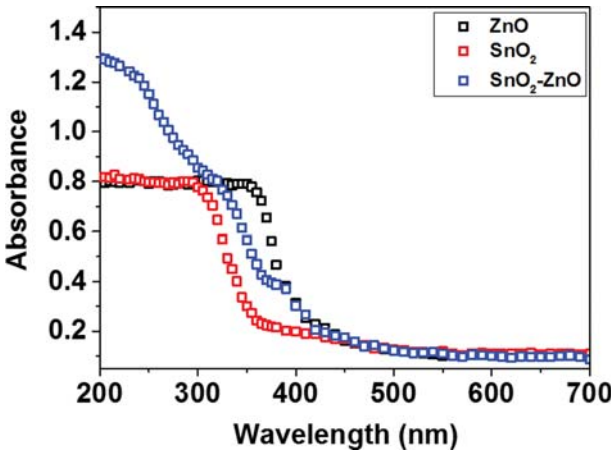

Fig. S5. UV-vis DR spectra of the (a) ZnO (b) SnO_2 and SnO_2-ZnO heterostructure.

two obvious absorption bands existed, which can be ascribed to the characteristic absorption of SnO_2 and ZnO. The appearance of two kinds of characteristic absorption bands confirmed that the SnO_2-ZnO nanocomposite consist of ZnO and SnO_2. Moreover, the absorption edge of SnO_2-ZnO nanocomposite was estimated as 390 nm, which corresponds to band gap energy of 3.18 eV, lower than those of both pure oxides. By combining the results of XRD, XPS, TEM, and UV-vis DR spectra, we concluded the formation of the SnO_2-ZnO heterostructure, therefore they are expecting to exhibit high photocatalytic efficiencies.

REFERENCES

1. W. Wang, Y. Zhu and L. Yang, *Adv. Funct. Mater.*, **17**, 59 (2007).